Sensitivity of Simulated Radiative Emission from Nitrogen Flows to Chemical Parameters

Kaelan B. Hansson * and Brett A. Cruden †
AMA Inc at NASA Ames Research Center, Mountain View, CA, 94035

Thomas K. West IV ‡
NASA Langley Research Center, Hampton, VA, 23681

Aaron M. Brandis§
NASA Ames Reseach Center, Mountain View, CA, 94035

Numerical models of hypersonic flows rely on chemistry data inferred from experiments and quantum calculations. Experiments from NASA's Electric Arc Shock Tube (EAST) measure the spectral emission of strong shocks in pure nitrogen flows. These spectral profiles are only approximately captured by numerical simulations. To address these discrepancies, one wishes to calibrate some of the chemical parameters to better match experiment. Because there are hundreds of parameters in the numerical model, a sensitivity analysis was carried out on the entire chemistry database to determine which parameters are most important to analyze in the future. In order to perform this work it was necessary to generate a consistent chemical database that interfaced with both the CFD and line-by-line radiation solver. Using Monte Carlo methods, the total Sobol index was calculated for important parameters. Twenty parameters were identified as important across the nitrogen system. However, it was noted that in some spectral regions, the parametric uncertainty was unable to bound EAST measurements. Further improvements could be made by increasing the parameter uncertainties or addressing other sources of modeling error.

I. Introduction

In hypersonic flight environments, accurate numerical predictions of heat flux, both convective and radiative, are necessary to design vehicles which will operate in these extreme conditions. To ensure this accuracy, models of hypersonic flows must be rigorously compared to experimental data. To probe the fine details of these conditions, spectroscopic measurements can provide density estimates of specific species, as well as a prediction of the level of excitation of the atoms and molecules. Numerically simulating an experimental spectra is one of the most granular means to carefully compare models. In order to predict the radiative signature (i.e. the spectrum) of a hypersonic flow, many chemical parameters must be used as inputs to the models. These parameters are necessary for the calculation of every property in the flow field, from bulk quantities, such as the viscosity and temperature, to the population of the excited states of each species.

Over the last several decades, accuracy in predicting radiative heating has improved by including models for an increasing number of physical processes. To define these models, though, an increasing number of physical parameters has been needed. Many of these parameters are based on experimental or legacy data which may not be accurate accross all regions of interest. This work is part of a larger effort which aims to calibrate these parameters across a range of flight regimes using modern experimental data. As will be shown, there are hundreds of parameters which must be assessed concurrently. This work is a preliminary sensitivity study to understand which parameters are most likely to be affected by the calibration.

Besides finding the most important parameters, one must ensure that the available model with a given parametric uncertainty can yield a prediction which matches the experimental data. With a perfect model, one expects that some combination of chemical parameters fits the experimental data across all conditions. However, in practice the numerical

*Research Scientist, Aerothermodynamics Branch.
†Senior Research Scientist, Aerothermodynamics Branch, and Associate Fellow AIAA.
‡Aerospace Engineer, Vehicle Analysis Branch, Systems Analysis and Concepts Directorate, Associate Fellow AIAA.
§Senior Research Scientist, Aerothermodynamics Branch, and Associate Fellow AIAA.

models employed make assumptions about the flow physics which may lead to inaccurate predictions regardless of the chemical parameters. Part of this work is to assess if model form discrepancies are significant.

Sensitivity analysis of this form has been performed before [1, 2]. However, these investigations focus on only the rates that were present in fluid models and usually on only one parameter in the rate equations. This analysis will investigate a larger number of parameters in each reaction as well as radiative and transport parameters. This will provide a more comprehensive and consistent view of which physical processes are dominant.

This paper begins with a discussion of the experimental spectroscopy data which motivates this investigation. This is followed by a brief discussion of the numerical modeling used to make a single prediction. A description of the tools needed to orchestrate an ensemble of models into a sensitivity analysis is then presented. This includes a new tool to sample a single chemical database and instantiate individual databases for each program in the modeling tool chain. An adaptive Monte Carlo method is also presented to extract the Sobol indices of the more important parameters with a reduced computational cost. The final part of the paper considers the resulting sensitivity analyses concurrently calculated across eight experimental conditions and ten spectral regions. The results show that the relative importance of various parameters tracks with intuitive expectations. Approximately 20 parameters are identified as the most important parameters for modeling a pure nitrogen shock wave. However,it is shown that the estimated uncertainties in the chemical parameters are not sufficient to bound the experimental measurements.

II. Review of Experimental Data

Hypersonic shockwaves at the Electric Arc Shock Tube (EAST) facility [3] are experimental datasets believed to provide new insight into chemistry models. EAST generates a traveling shock using a high voltage discharge. The shock is imaged using several high speed cameras and spectrometers as it passes through the test section. The cameras are named VUV, Blue Red and IR for the approximate spectral ranges they image. Each camera produces a single two dimensional dataset, the intensity as a function of position and wavelength. Note that the shock is always assumed to be one dimensional.

The Test 62 campaign at EAST investigated pure nitrogen shocks at a range of velocities. The pressures in all cases were 0.2 Torr. Of the 42 runs, eight were selected for analysis. These eight covered the velocity range of the campaign and exhibited the highest quality spectral data. However, each shot used different camera configurations in the campaign to probe specific spectral features. Table 1 summarizes the data used in this analysis.

EAST data has been used to validate radiative heating for flight environments. For an analysis of heat flux, it is common to integrate the camera data over some large spectral range. However, in this work, the individual features of the spectral are probed. Individual regions in the position-wavelength image are considered separately. These regions are taken from Brandis et al. [4] which were identified as regions where other effects (e.g. impurities) would not influence the data. Due to the nature of the numerical technique employed (discussed in Section III.A), the shock front cannot be accurately modeled. Instead the spectra is analyzed in the spatial positions from 0.5 to 1.0 cm behind the shock. Because the EAST data used differing camera settings across the various runs, not all regions are comparable to experiment, as some spectral regions may be outside of a particular run's camera settings.

For each region, two different analyses are performed to compare numerical models to the EAST data. The first is to compare the integrated intensity over the spectral region, and the second is to calculate a log-likelihood for the region.

Integrated Radiance: For the integrated approach, the intensity is integrated over the wavelength range and then averaged over the position range of the particular region. The integral of the EAST data and the numerical data can be directly compared.

Log-Likelihood: A likelihood is a probability that the numerical data matches the experimental data given some uncertainty in the model or the measurement. This is the same metric used for Bayesian analysis to generate a posterior. To calculate the likelihood, it is assumed that the pixel grid used by EAST and the numerical data are the same. Each pixel is the assumed to be independent. A probability density function (PDF) is constructed for the expected error of each pixel. For this work, each pixel is given a truncated normal distribution. The most likely value is the EAST intensity and the standard deviation is twice the EAST pixel value. An example of these pixel PDFs is given in Fig. 1. Note, for numerical precision, the PDF stored is the natural logarithm of the PDF. To calculate the likelihood of any pixel, one simply evaluates the PDF at the numerically simulated intensity of the pixel. To calculate the likelihood of the entire region, one takes the product of the likelihoods across all pixels in the region. In log space, this is equivalent to a sum of the log-likelihoods of each pixel in the region.

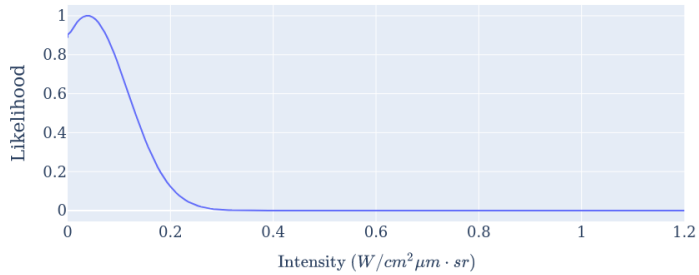

(a) The normalized PDF of intensity of a single pixel from the EAST data. Here the standard deviation is assumed to be twice the most likely value

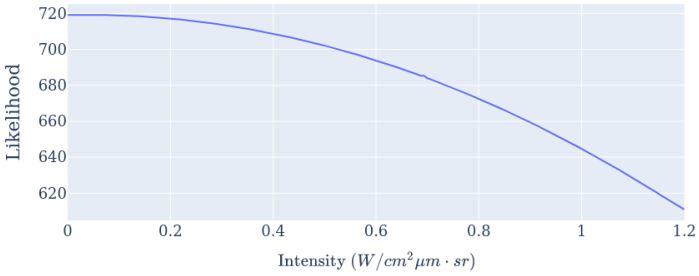

(b) The log of the PDF with an additional offset to account for the dynamic range. This is stored at each pixel value for the log likelihood calculation

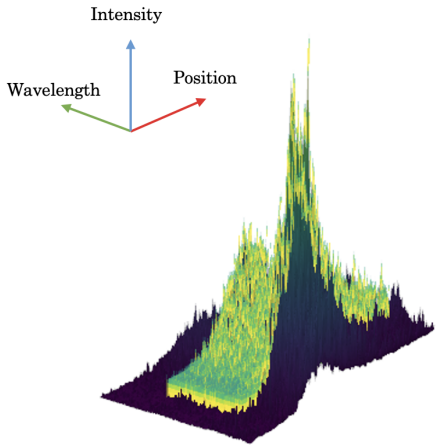

(c) The original EAST data in purple represented as a manifold in position-wavelength-intensity space with the three dimensional likelihood data represented as the yellow cloud

Fig. 1 Representation of the data which must be precalculated for the log-likelihood calculation (Section II). At each pixel, an independent probability distribution function must be generated to describe the uncertainty in the measurement. This is shown in Subfigure 1a. Due to numerical precision, it is more robust to store the logarithm of the PDF (Subfigure 1b). As one accumulates these distribution functions they can be stored as a volume dataset: probability density as a function of position, wavelength, and intensity. This is represented in Subfigure 1c along with the original EAST data as a surface in that space.

			Camera Ranges [nm]			
Shot Number	**Velocity [km/s]**	**Pressure [Torr]**	**VUV**	**Blue**	**Red**	**IR**
42	5.94	0.2	117 - 173	183 - 357	468 - 889	1121 - 1709
40	6.86	0.2	143 - 198	323 - 497	468 - 889	837 - 1439
13	8.13	0.2	142 - 198	323 - 497	409 - 940	811 - 1443
6	8.71	0.2	142 - 198	323 - 497	409 - 940	811 - 1443
5	9.54	0.2	142 - 198	323 - 497	409 - 940	811 - 1443
19	10.31	0.2	142 - 198	323 - 497	467 - 889	837 - 1439
23	10.71	0.2	117 - 173	183 - 357	653 - 659	1121 - 1699
20	11.14	0.2	142 - 198	323 - 497	409 - 940	829 - 1439

Table 1 Summary of the eight shocks used in this work. For each shock a spectrally resolved sensitivity analysis is performed

III. Methods

The sensitivity analysis treats the numerical model of the shock as a pure function of one vector of data (the inputs) producing another vector of data (the outputs). The inputs are the chemical parameters, which are sampled repeatedly. The output for each sample is an array of calculated radiances and log likelihoods over the pre-selected wavelength ranges and spatial positions. A single sample is calculated in a two step process. First, a fluid simulation is performed, which calculates a field of temperatures and number densities. Second, a line-by-line radiation solver is used to calculate the spectrum of this field. The following sections cover the particulars of these two simulations followed by a discussion of the framework used to sample the chemical rates and process the generated data.

A. Fluid Solution - DPLR

The fluid solver used in this analysis is DPLR [5], a hypersonic solver used extensively at NASA Ames. DPLR implements the non-equilibrium thermodynamics that are used for flight environment predictions for NASA missions. Often for analysis of shockwaves, DPLR's line relaxation algorithm is used on a sphere or cylinder geometry. The stagnation line is taken to be analogous to a moving shock in EAST. However, due to computational limits, this work uses the space marching feature in DPLR to rapidly calculate one dimensional shock wave predictions.

Space marching is a simplified technique for simulating a one dimensional normal shock. The method uses the inviscid flow assumption to directly integrate the inviscid fluxes of the reacting Euler equations in space. The simulation is initialized by the Rankine-Hugoniot jump conditions for a normal shock. The only processes which change in space are the chemical source terms which come to equilibrium as the simulation proceeds away from the shock.

In section III.B, the line-by-line solver is described. The last step in its calculation is the spatial and spectral convolution of the intensities with a series of functions representing the broadening processes present in the EAST facility. Most space marchers only produce data in the subsonic region of the flow, but in order to accurately calculate the spatial broadening, it was necessary to pad the supersonic region with points containing the free stream state. This can be see in the bottom portion of Fig. 2.

B. Radiative Calculations - NEQAIR

The results from DPLR are used as inputs into NEQAIR, a code developed by NASA Ames over the last several decades [6], in "shock tube mode." NEQAIR analyzes the radiation on one or more lines of sight (LOS), which are one dimensional sets of densities and temperatures. This data is used to calculate the spectral emission and absorption coefficients at each point using a line-by-line method. Various modes can then be used to either integrate the radiance along the line, or compute the radiance perpendicular to the LOS (shock tube mode).

In order to calculate the spectra, NEQAIR must estimate the density of excited states of each species at an individual LOS point. For this work, the quasi steady state (QSS) approximation is used to generate a non-Boltzmann distribution of states. The QSS calculation is dependent on a database of species levels, emission lines, and rates of excitation and decay. Once the excited state densities are estimated, NEQAIR directly calculates the emitted spectrum from each cell using a local escape factor approximation. Lastly, NEQAIR performs a convolution of the spatial and spectral intensity to match the measured broadening functions of the EAST facility.

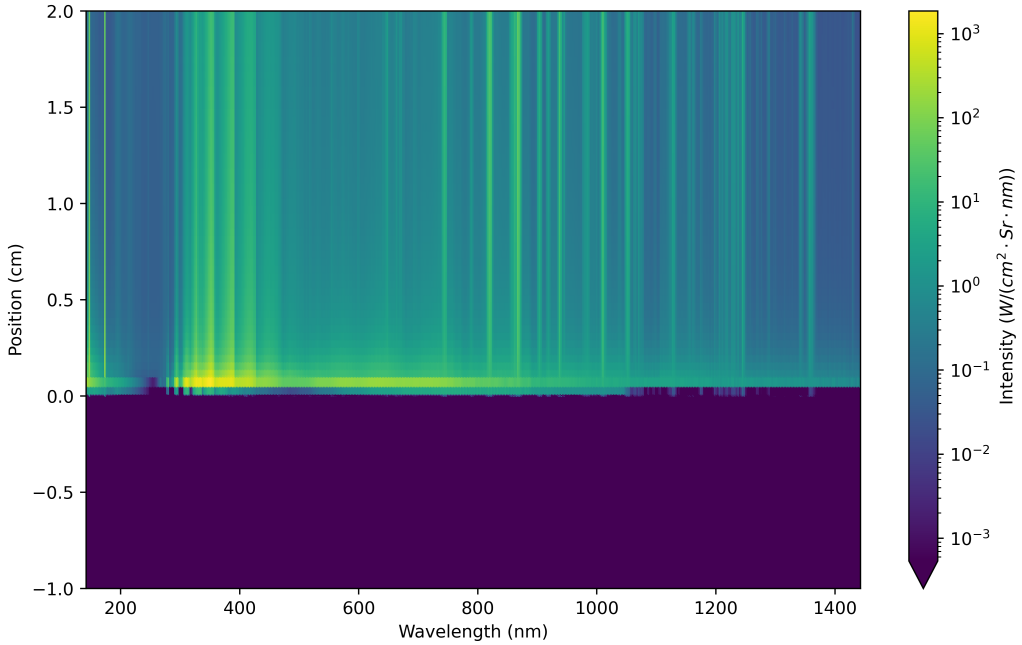

Fig. 2 NEQAIR output for single realization. Input data generated using the space marcher mode of DPLR. Regions of this output are integrated to form the final output vector.

The final result from these calculations is a two dimensional array of intensities as a function of wavelength and position. An example of this data is shown in Fig. 2. When performing the log-likelihood analysis described in Section II, a further post processing step must be applied to exactly match the pixel grid in EAST. The NEQAIR output is taken as node centered data, with linear interpolation between the points while EAST measures cell centered pixels. To perform this processing, the NEQAIR data is over-sampled onto a grid of the EAST pixel corners combined with the original NEQAIR grid, then each pixel is integrated by the trapezoid rule.

C. Sensitivity Analysis

1. Database Creation

The practical challenge of this sensitivity analysis is coordinating the chemical parameters and correctly distributing them to the specific chemical databases needed for each individual simulation tool. The databases used by DPLR and NEQAIR use a variety of chemical data. DPLR uses properties such as transport properties, reaction rates, and vibrational relaxation times while the NEQAIR databases contain state specific properties such as excitation rates, cross sections, and Einstein coefficients. Ideally, these databases would be independent and could then be sampled independently. However, there is some data used in both codes which must be sampled consistently between the two databases.

DPLR requires a variety of chemical data for each species. This includes Gupta transport properties [7, 8], vibrational relaxation times [9, 10], and chemical reactions. The reactions are parameterized using the modified Arrhenius form.

$$k_f = AT^{\eta} e^{\frac{-E_a}{kT}} \tag{1}$$

where k_f is the forward reaction rate, A is the prefactor, η is a non-dimensional exponent, T is the temperature, E_a is the activation energy, and k is the Boltzmann constant. The parameters varied are the prefactor, A and the exponent η (at times written out as 'eta'). For this work, the sampling of the databases is done on a different temperature scale. One can write Eq. 1 as

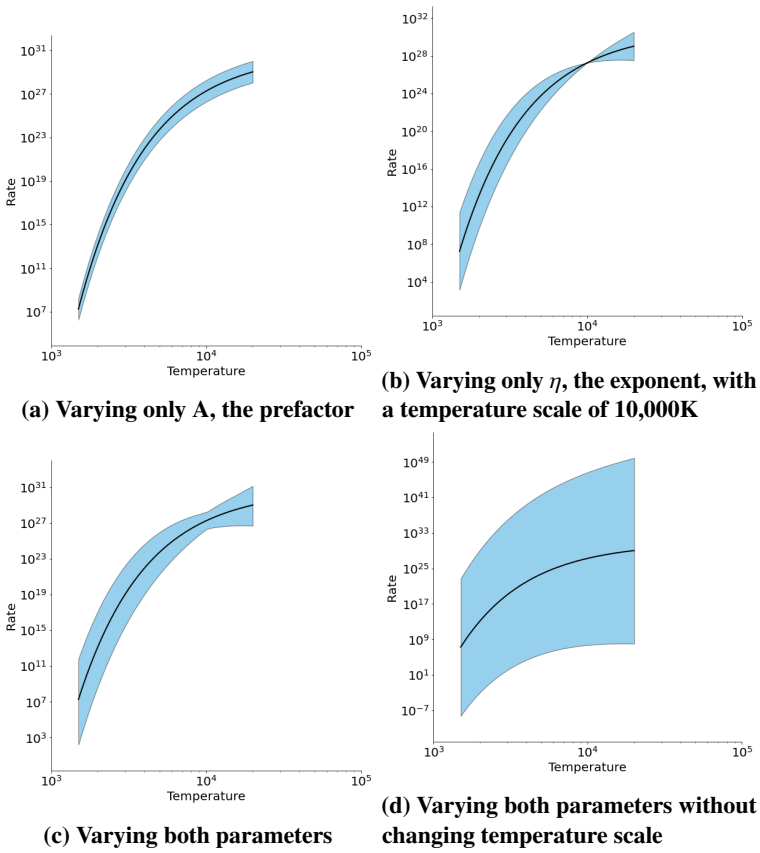

(a) Varying only A, the prefactor

(b) Varying only η, the exponent, with a temperature scale of 10,000K

(c) Varying both parameters

(d) Varying both parameters without changing temperature scale

Fig. 3 Schematic representation of the how the variation in the modified Arrhenius parameters of Eq. 2 affect the temperature dependence of the rate constant, k_f. The nominal rate constant is given as the black curve while the blue region represents the support of the rate constant under all possible samplings of the prefactor and the exponent. By changing the form to have the term $\left(\frac{T}{10000K}\right)^{\eta}$, the variance in η leaves a cusp at the 10000 Kelvin point, as opposed to zero Kelvin.

$$k_f = A' \left(\frac{T}{10000K}\right)^{\eta} e^{\frac{-E_a}{kT}} \tag{2}$$

where $A' = A \cdot (10000K)^{\eta}$. This conversion can be done on a nominal rate without any loss of generality. However, once one samples in this A' - η space, the resulting distributions are different. In this form, any changes in η appear to "rotate" the reaction about its value at 10,000 Kelvin instead of zero. Fig. 3 shows a schematic of this effect. Having the reactions grounded around 10,000K corresponds to the intuition that nominal rates (by Park [10]) were developed for shock at these temperatures. The greater uncertainty in the rate constant should be at low temperatures or much higher temperatures. Varying η in this way captures this effect.

Beyond the forward reaction rate, there are other parameters in DPLR's reaction mechanism. The temperature above is a function of the mode specific temperatures in DPLR's two temperature model:

$$T = T_t^{n-1} T_v^n \tag{3}$$

where T is the temperature used in Eq. 1, T_t is the translational or kinetic temperature, T_v is the vibrational temperature and n is a constant that can take on values between zero and one. Generally this parameter is given a nominal value of either 0.0 or 0.5; for this analysis all reactions for which n is nominally 0.5 vary n between 0.3 and 0.7. DPLR's reaction model also provides an additional energy distribution term, h_{0frac} which varies the distribution of chemical energy in a reaction to the various modes. For example, in an electron impact ionization reaction, DPLR by default adds 28% of the

reaction energy to the free electron mode, which is lumped with the vibrational modes [8]. h_{0frac} is adjustable for all reactions and is varied as well.

The NEQAIR database holds significantly more data than DPLR. NEQAIR uses state specific rates to calculate the excited state populations and emission constants. This includes electron impact ionization, and dissociation cross sections, modified Arrhenius rates for electron impact excitation, heavy particle quenching rates, and pre-dissociation times. Because some of these parameters were hard-coded, changes were made to NEQAIR to allow for a greater parametric flexibility. First, the original heavy particle quenching rates were written as a modified Arrhenius rate with $\eta = 0.5$ exclusively. Now, the η can be and is varied. The heavy particle dissociation rates were also categorized by only atomic and molecular partners. Now these rates can be specified by individual species, allowing an exact match to DPLR's reaction mechanisms.

Because both the NEQAIR and DPLR databases are regenerated at each sample, one can ensure that the same rates are used for the heavy particle dissociation rates in both DPLR and NEQAIR. This consistency is valuable for having confidence in the combined software system as a whole. However, there are still some mechanisms which are not necessarily consistent. For example, the state specific electron dissociation rates in NEQAIR are not combined into a single lumped rate which is used in DPLR.

2. Adaptive Monte Carlo

The chemistry databases analyzed in this sensitivity analysis contain hundreds of parameters. To perform a standard Monte Carlo analysis would be prohibitively expensive, as the total number of simulations is proportional to the product of the number of parameters times the number of samples needed to converge the solution. However, if one only wishes to converge some smaller number of parameters and leave higher uncertainty for unimportant parameters, one can reduce the total number of calculations.

In a standard calculation of the Sobol indices [11, 12], one calculates two vectors of input samples, A and B. Then one evaluates the function at $a \in A$ and at $a_k \in AB_k$, where AB_k are the parameters from A except the kth parameter is taken from B. The total Sobol indices are then:

$$S_t = \frac{var\left(f(a_k) - f(a)\ for\ a_k, a \in AB_k, A\right)}{var\left(f(a)\ for\ a \in A\right)} \tag{4}$$

where S_t is the total Sobol index, var is the variance, and f is the function to be evaluated. The error in this evaluation is inversely proportional to the number of samples and can be evaluated using bootstrap methods.

The Sobol index of the kth parameter can be expressed as the ratio of two variances. The first (the denominator in Eq. 4) is the total variance of the function over the sample space and the other (the numerator in Eq. 4) is the total variance of difference for the function evaluated at any two points aligned in the kth direction. This second variance must be less than or equal to the first. Furthermore, it is assumed that the sampling errors of the two variances are bounded by the sampling error of the variance of the samples from A. This means that if one knows the variance of the function evaluations of A to some error ϵ, one expects that AB_k will require no more evaluations than the length of A to reach the same error.

Thus, the adaptive Monte Carlo proceeds in two steps. The matrix A is generated by multiple Latin hypercube evaluations of the sample space (usually 200 samples) until the total error of the variance of the output variables is reduced to a threshold of 2%. The matrix AB is generated for all parameters with a small number of samples. The number of samples selected must be sufficient to gather meaningful bootstrap statistics, but not computationally intractable. Reasonable results were generated with eight starting samples. The Sobol indices are then calculated as well as their bootstrap errors (calculated at one standard deviation), and then the most important five are selected. All parameters whose Sobol index error bound does not overlap the error bounds of the most important parameters are dropped from the analysis. The sampling only continues for parameters that retain some possibility of importance.

IV. Results

For the eight EAST cases discussed in Section II, a sensitivity analysis is performed on each of the ten spectral regions of interest. The analysis is duplicated both for the integrated intensity as well as the log-likelihood for each region. The complete set of results for the 160 datasets cannot be displayed here. The results are organized in three parts and are selected to highlight features of the physics and experimental comparisons. First, the total Sobol indices of only the integrated radiances of each region are presented. This data is independent of the EAST results and can be used to probe the behavior of the DPLR-NEQAIR model. Second, a comparison is made between the sensitivity analysis

based on the integrated radiance vs. the log-likelihood. Lastly, histograms of the sampled data are presented to show a comparison of the spread of the numerical data against the EAST measurements.

Figures 4 to 8 display the results of the sensitivity analysis for each spectral region in Test 62, Shot 6. This case was the median shock velocity of the runs investigated. Abbreviated parameter names are used in the figures and can be looked up in Table 2 for a detailed description. One can see that the total Sobol indices are not the same nor do they have the same distribution across each spectral region. This is expected, as each spectral region emits from different species and different excited states which are formed from differing chemical pathways. What is perhaps more notable is that the four most important parameters from each region are parameters from the DPLR model. In particular, the prefactors for the nitrogen molecule dissociation reaction feature prominently with partners N and $e-$.

Given that the particular partner reactions are the most important, one can extract the prefactors of each dissociation reaction and plot those Sobol indices as a function of the shock velocity. In Fig. 9 one sees the expected trend: at low speeds the dissociation is low and is driven by molecule-molecule impacts. As the dissociation increases with shock speed the atomic and electron densities increase and drive the dissociation process. At 11 kilometers per second, the electron impact dissociation process is dominant. An implication of this result is that the inconsistency in the electron impact dissociation rate between NEQAIR and DPLR (NEQAIR has a state-specific rate which is not necessarily equivalent to the lumped rate in DPLR) must be resolved.

Since the electron dissociation process becomes dominant, one may believe that at high speeds the ionization processes are in fact more important than any of the dissociation processes. Fig. 10 shows the Sobol index for the prefactor of several dissociation and ionization reactions. One can see that the $N + e \longleftrightarrow N^+ + 2e$ reaction dominates above ten kilometers per second. Curiously, atomic heavy particle ionization is never a dominant mechanism.

For any spectral region, Sobol indices are generated for two output variables, the integrated radiance and the log-likelihood compared to the EAST data at that region. Two examples of these Sobol indices are plotted in figures 11 and 12. There is striking similarity between the two distributions until one reaches parameters of very low Sobol index. This means that the individual features, which are captured only in the log-likelihood metric are unimportant relative to the level of change in an overall sense.

Finally, in addition to calculating the Sobol indices of the parameters, it is helpful to plot a histogram of all values of the integrated radiance at a given region against the spread of all chemical parameters. This can also be directly compared to EAST data. For example, Fig. 13 shows a spectral region from Shot 13 in the Blue region. Here the spread of the numerical data contains the EAST measurement. However, Fig. 14 shows a region from the VUV camera for the fastest run, Shot 20. Here one can see that the EAST data is approximately half an order of magnitude above any value seen in the numerical predictions. This immediately implies that no Bayesian calibration is possible given the current prior.

There are three possible explanations for this discrepancy. One, the uncertainty in the EAST measurement is such that if a PDF of the integrated EAST data were generated, it would in fact overlaps with the predictions. Two, the estimated uncertainty bounds are too narrow. Three, the model itself is not capturing sufficient physics and given a priori correct chemical parameters, would still miss the EAST data regardless (in this case because the space marcher ignores viscous effects, disregards multidimensional effects and neglects shock deceleration effects [13]). Of these options, the first is ruled out based on previous error analysis of the EAST facility. There is no other present information to make either of the remaining options more valid than the other. It is expected that the uncertainties used could be justified to have larger bounds, but it is unknown if such a change would circumscribe the data. Furthermore, it is unclear that even if the chemical parameters did bound the data that there would be a single set of parameters that consistently matched experimental data at all conditions. One is left to conclude that both a model error and overly conservative uncertainties could be present.

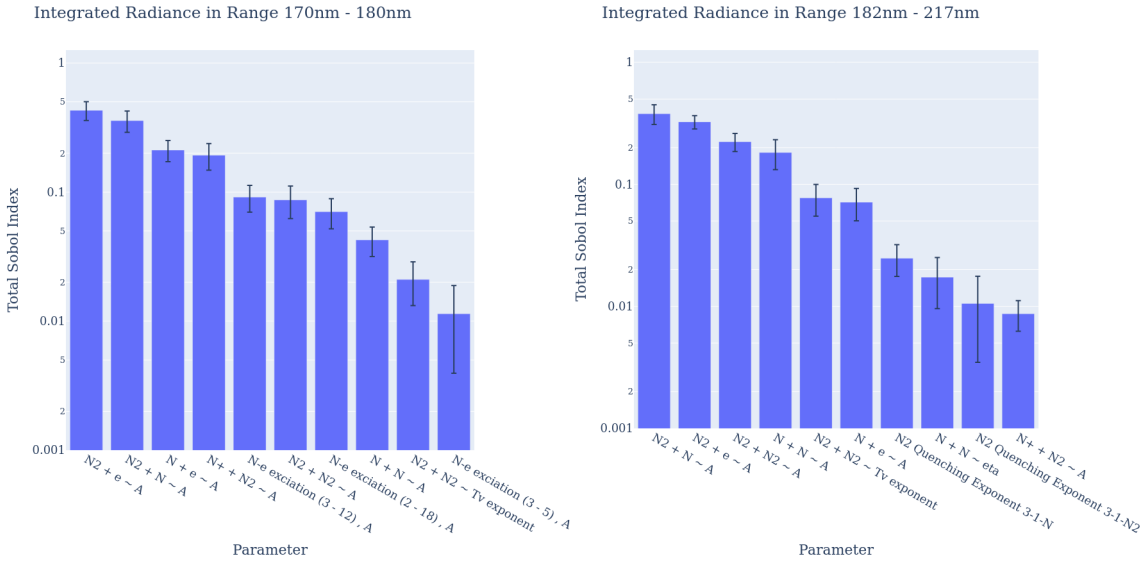

Fig. 4 Sensitivity analysis for the VUV regions of EAST Test 62, Shot 6, with a Shot velocity of 8.71 km/s. The output variable is the integrated radiance in the marked wavelength range averaged between 0.5 and 1.0 cm behind the shock. The descriptions to parameter names are given in Table 2

.

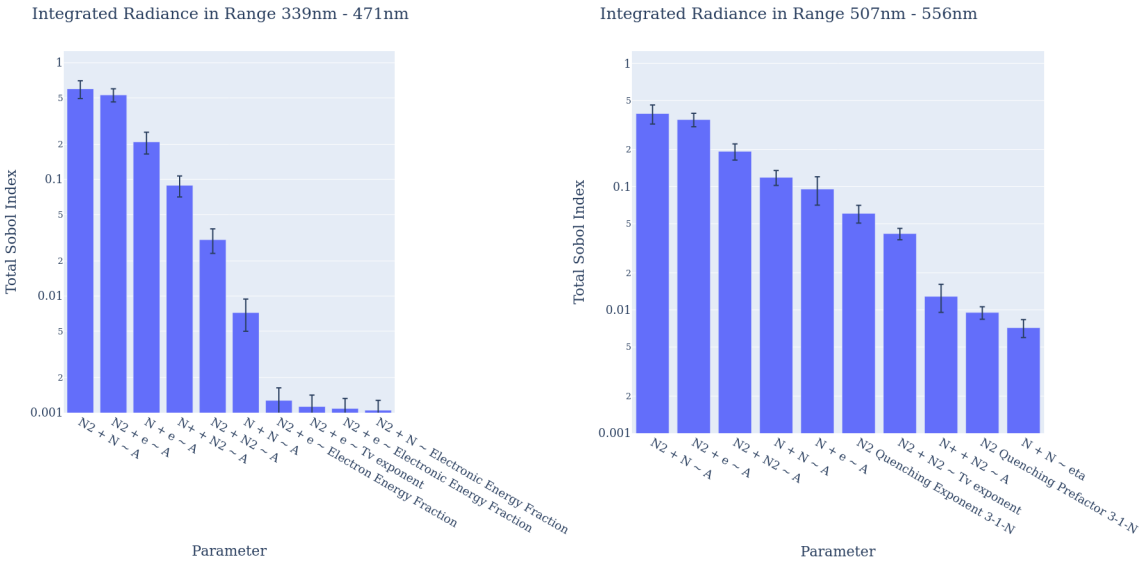

Fig. 5 Sensitivity analysis for all regions of Shot 6, continuing from Figure 4.

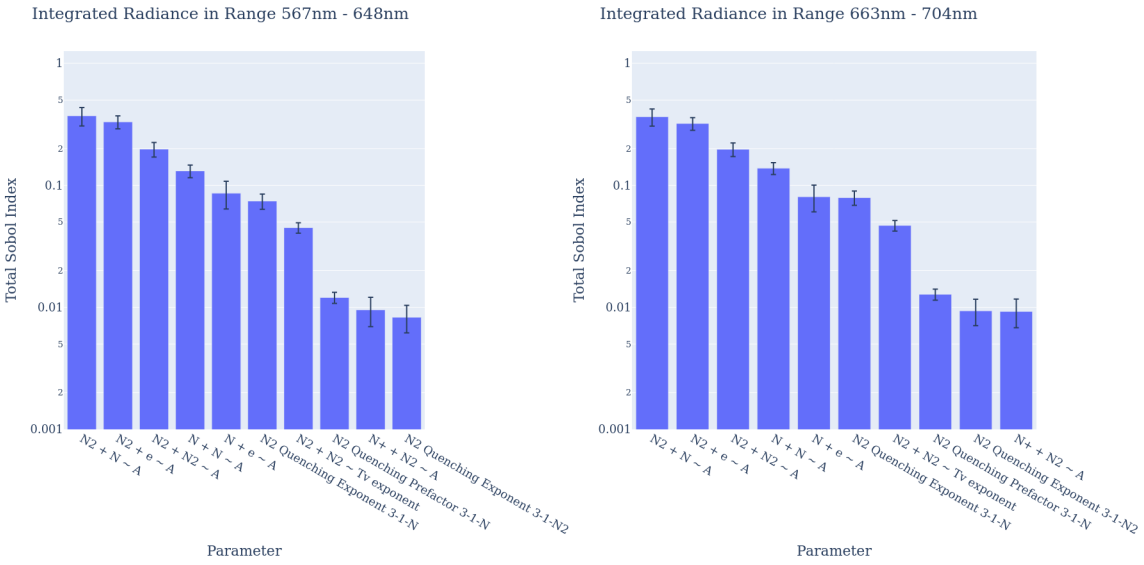

Fig. 6 Sensitivity analysis for all regions of Shot 6, continuing from Figure 4.

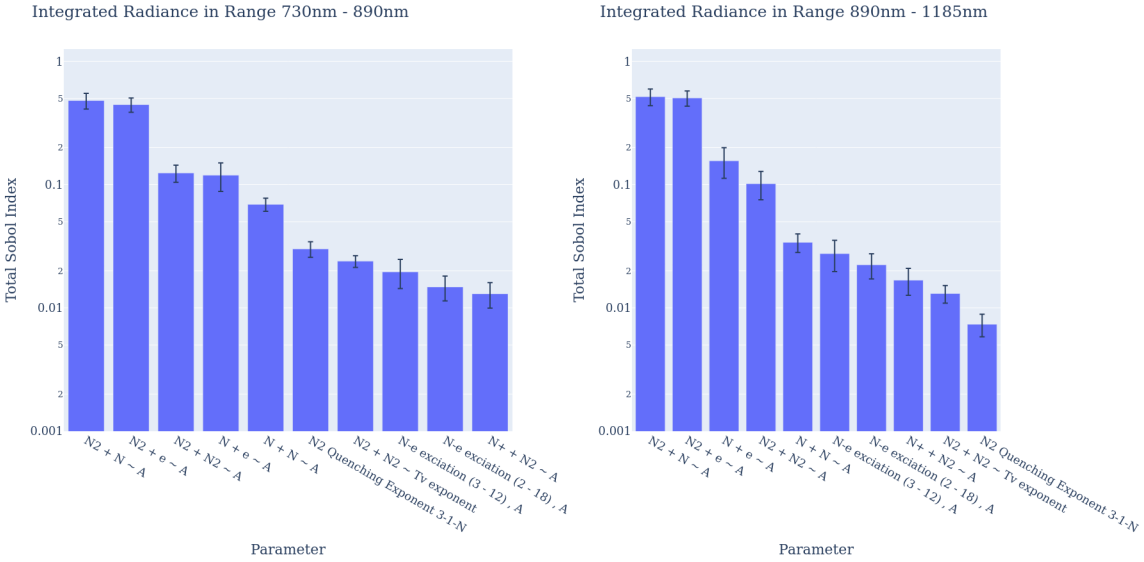

Fig. 7 Sensitivity analysis for all regions of Shot 6, continuing from Figure 4.

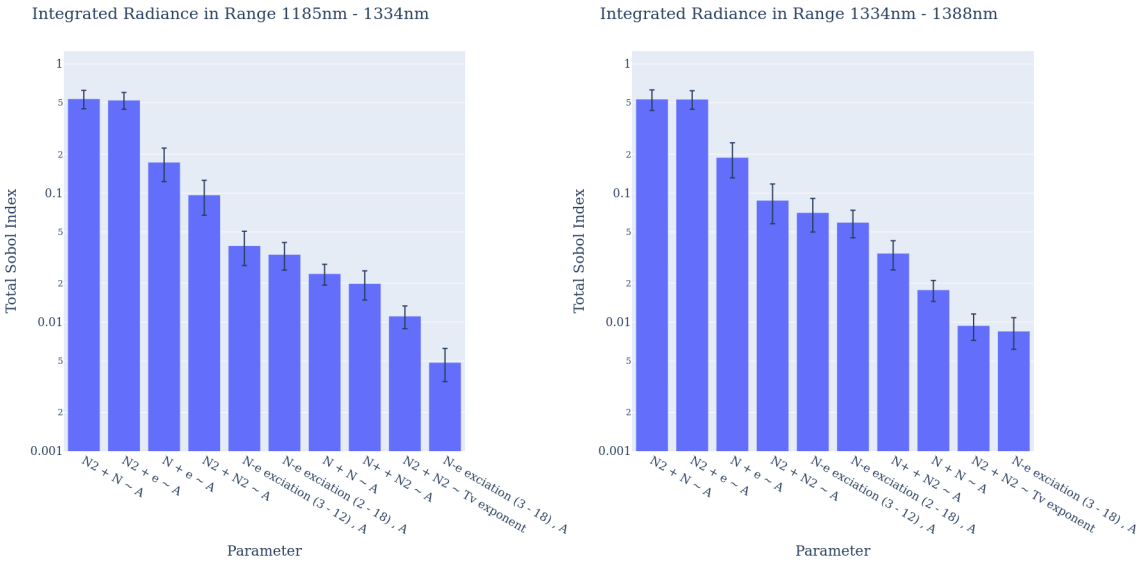

Fig. 8 Sensitivity analysis for all regions of Shot 6, continuing from Figure 4.

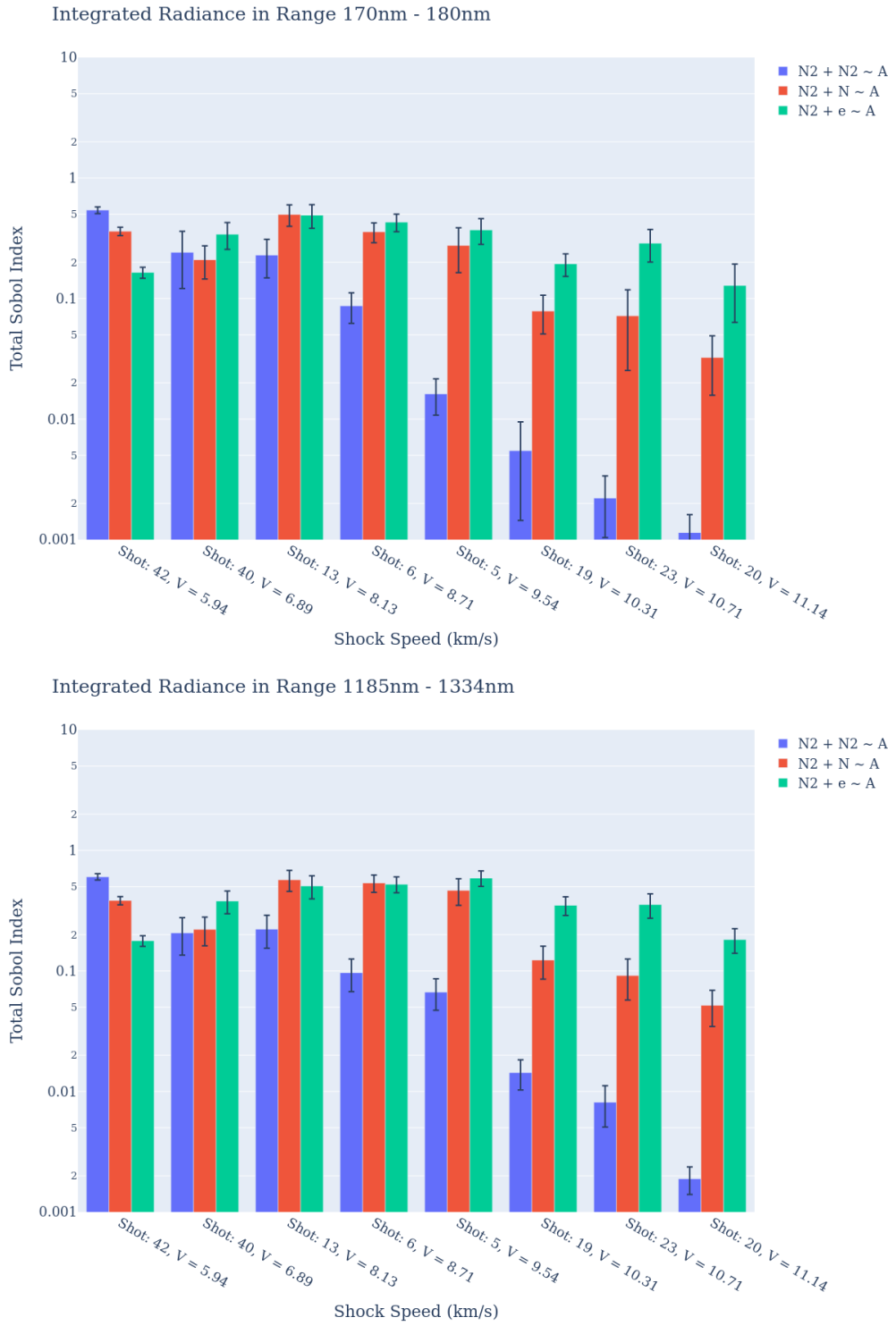

Fig. 9 Comparison of Sobol indices for three chemical parameters taken from different shots, organized by shock velocity. The three parameters highlight the relative importance of different third bodies in the dissociation reaction. At low speeds the $N_2 - N_2$ reaction dominates while at high speeds electron impact dissociation becomes dominant. This corresponds to the chemical distribution at these higher speeds

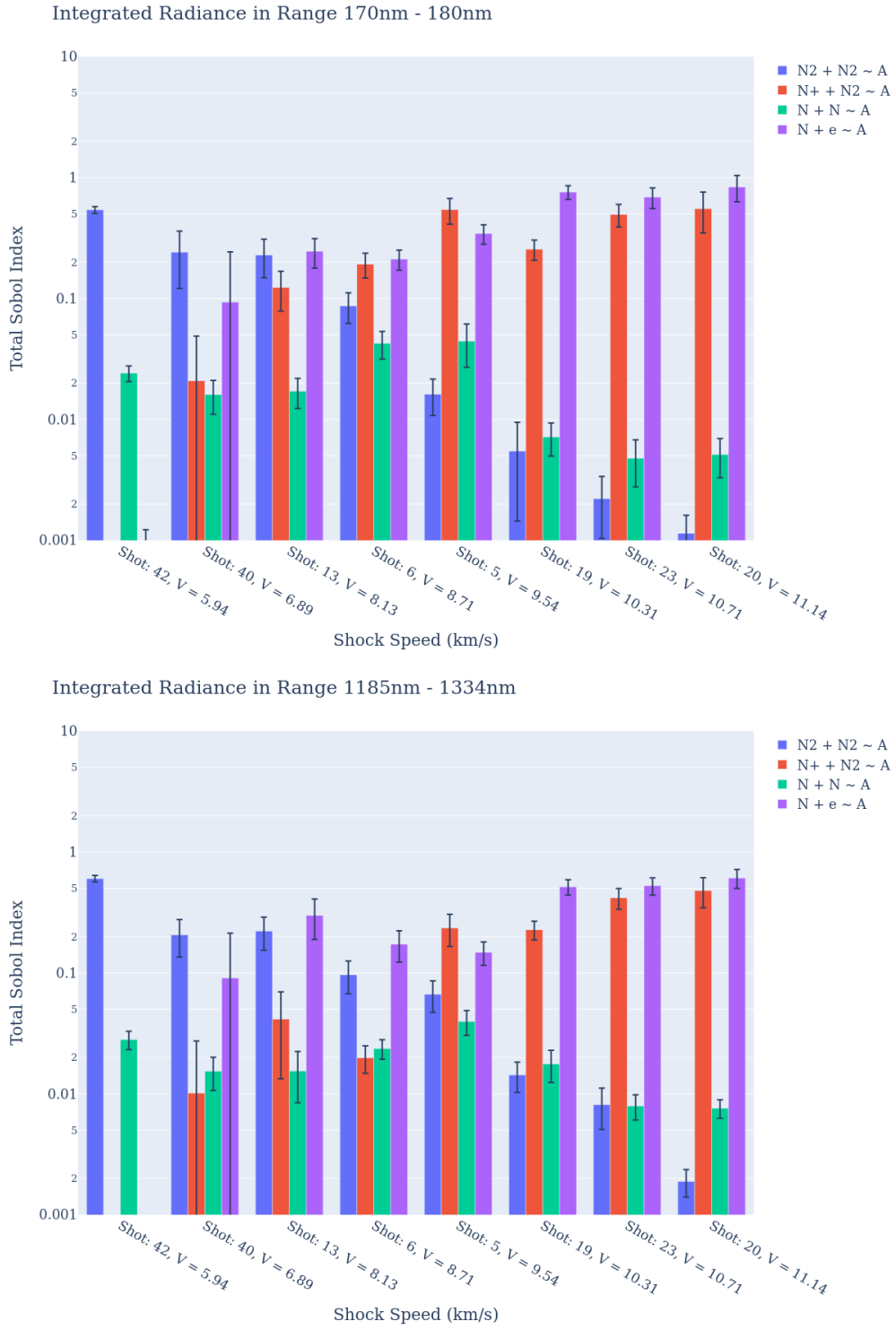

Fig. 10 Comparison of Sobol indices for three chemical parameters taken from different shots, organized by shock velocity. The three parameters compare the importance of dissociation, heavy particle ionization, and electron impact ionization.

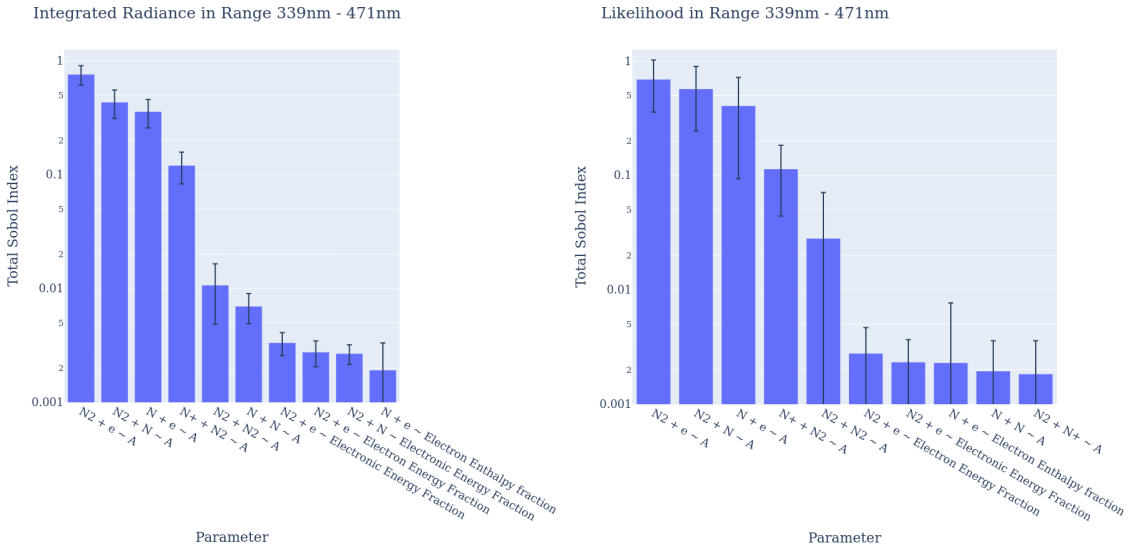

Fig. 11 Comparison of Sobol indices for EAST Shot 5 at the same spectral region using two different metrics: an integrated radiance and a log likelihood. One can see that the most parameters are the same between the two analyses for all but the lowest Sobol index parameters shown.

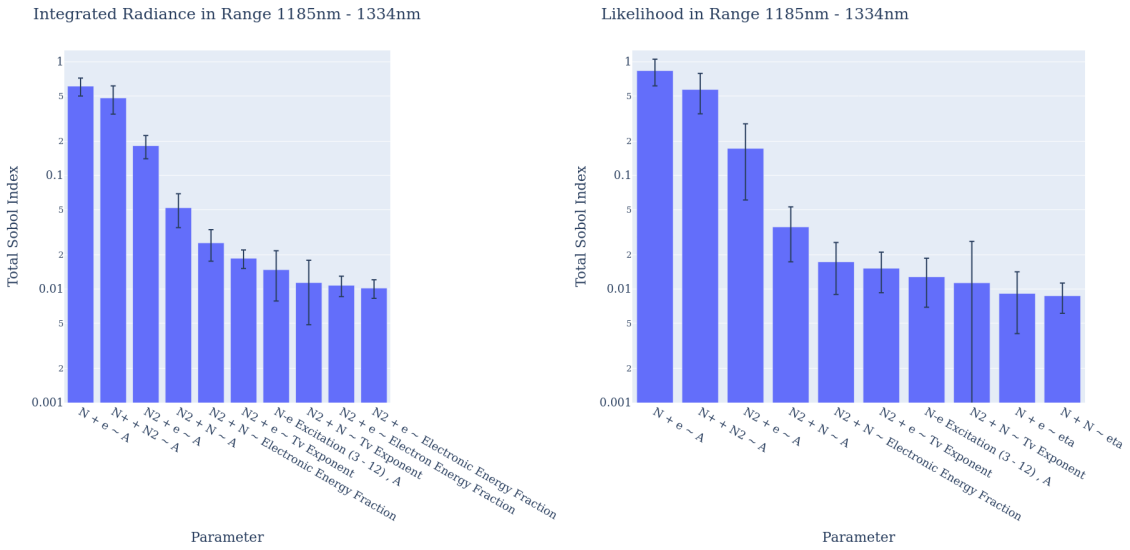

Fig. 12 Comparison of Sobol indices for EAST Shot 20 at the same spectral region using two different metrics: an integrated radiance and a log likelihood. One can see that the most parameters are the same between the two analyses for all but the the lowest Sobol index parameters shown.

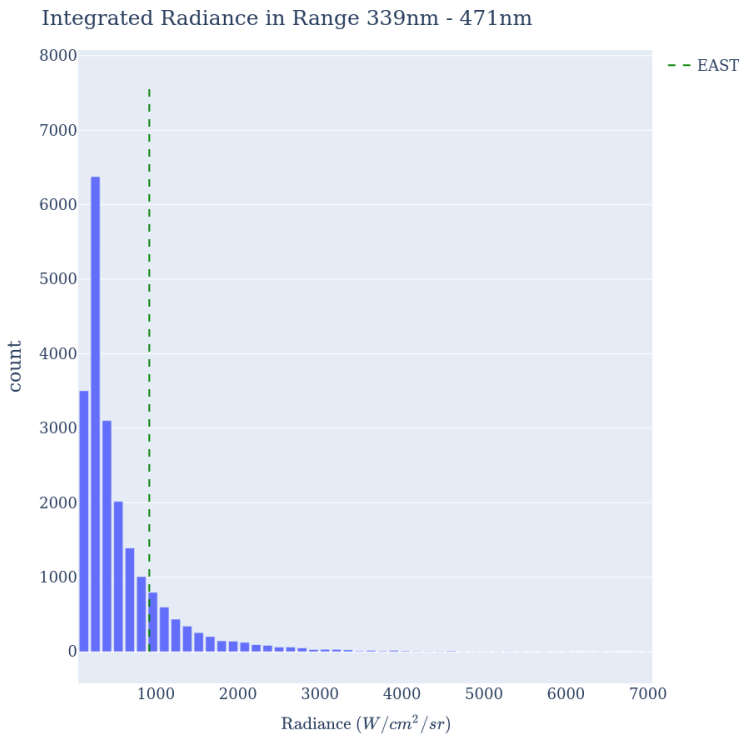

Fig. 13 Histogram of the predicted integrated radiance from Shot 13 (8.13 km/s) of the EAST dataset in the Blue region. The experimental data is shown by the green line. One can see that the experiment is bounded by the spread of the chemical parameters.

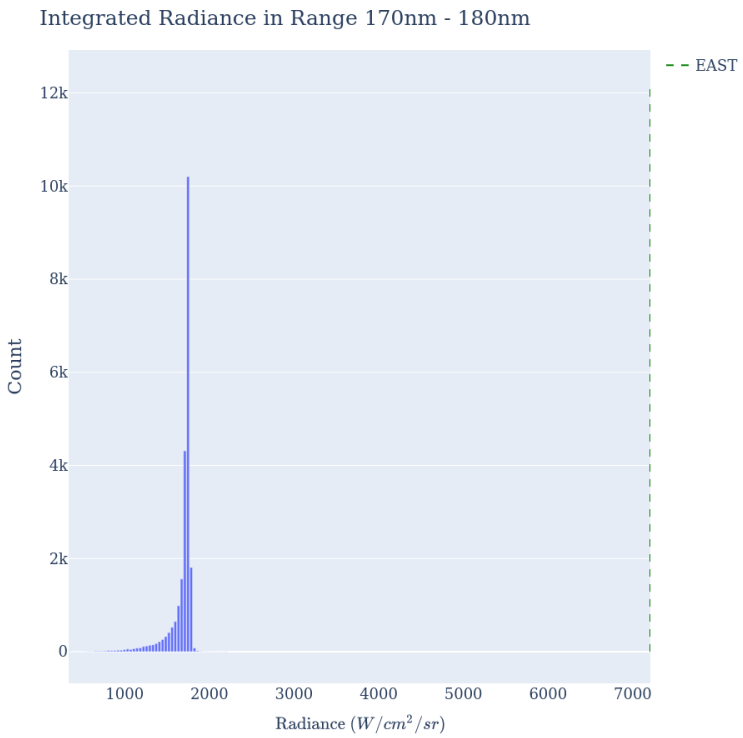

Fig. 14 Histogram of the predicted integrated radiance from Shot 20 (11.14 km/s) of the EAST dataset in the VUV region. The experimental data is shown by the green line. DPLR and NEQAIR under predict the radiance under all sampled combinations of chemical parameters.

Table 2 Descriptions of the parameters used in the sensitivity study as well as associated bounds. The first column corresponds to the names of the top five most important parameters in Figures figs. 4 to 8. The last column shows the ranges of the parameters as a pair of values. The first value is the nominal parameters used in the DPLR/NEQAIR databases. The second identifies sampling range around the nominal parameters. Parameters that are varied geometrically have uncertainties given as percentages, and cannot take on negative values. Uncertainty that are varied arithmetically are given in absolute units. One-sided arithmetic distributions may be expressed with only a positive error bound to avoid taking on negative values. (E.G. 0.0 + 0.5 is the range from 0.0 to 0.5 with a nominal value of zero.)

Parameter Key	Description	Range
$N_2 + e$~A	The prefactor of the modified Arrhenius rate for the reaction $N_2 + e \rightarrow 2N + e$	$1.2 \cdot 10^{22}\ m^3/s/kmol$ +/- 1000%
$N_2 + e$~T_v Exponent	For the Park Temperature $T = T_t^{1-n} T_v^n$. n is varied.	0.5 +/- 0.2
$N_2 + e$~Electronic Energy Fraction	The fraction of energy given to electronic modes post collision for $N_2 + e^- \rightarrow N + N + e^-$	0.0 + 0.1
$N_2 + e$~Electron Energy Fraction	The fraction of energy given to free electron post collision for $N_2 + e^- \rightarrow N + N + e^-$	0.0 + 0.1
$N_2 + N$~A	The prefactor of the modified Arrhenius rate for the reaction $N_2 + N \rightarrow 3N$	$3 \cdot 10^{19}\ m^3/s/kmol$ +/- 1000%
$N_2 + N$~Electronic Energy Fraction	The fraction of energy given to electronic modes post collision for $N_2 + N \rightarrow N + N + N$	0.0 + 0.1
$N_2 + N2$~A	The prefactor of the modified Arrhenius rate for the reaction $N_2 + N_2 \rightarrow 2N + N_2$	$7 \cdot 10^{18}\ m^3/s/kmol$ +/- 1000%
$N_2 + N_2$~T_v Exponent	For the Park Temperature $T = T_t^{1-n} T_v^n$. n is varied.	0.5 +/- 0.2
$N + e$~A	The prefactor of the modified Arrhenius rate for the reaction $N + e \rightarrow N^+ + 2e$	$2.5 \cdot 10^{31}\ m^3/s/kmol$ +/- 1000%
$N + e$~Electron Energy Fraction	The fraction of energy given to free electron post collision for the reaction $N + e \rightarrow N^+ + 2e$	0.0 + 0.1
$N + +N2$~A	The prefactor of the modified Arrhenius rate for the reaction $N^+ + N_2 \rightarrow N + N_2^+$	$1 \cdot 10^9\ m^3/s/kmol$ +- 1000%
$N + N$~A	The prefactor of the modified Arrhenius rate for the reaction $N + N \rightarrow N + N^+ + e$	$4.4 \cdot 10^4\ m^3/s/kmol$ +- 1000%
$N + N$~eta	The exponent of the modified Arrhenius rate for the reaction $N + N \rightarrow N + N^+ + e$	1.5 +/- 0.5
$N - e$ Excitation (2 – 18), A	The prefactor of the modified Arrhenius rate for the reaction $N(2) + e \rightarrow N(18) + e$	$1.30 \cdot 10^{-8} cm^3/s/part.$ +/- 1000%
$N - e$ Excitation (3 – 12), A	The prefactor of the modified Arrhenius rate for the reaction $N(3) + e \rightarrow N(12) + e$	$7.30 \cdot 10^{-6} cm^3/s/part.$ +/- 1000%
$N - e$ Excitation (3 – 5), A	The prefactor of the modified Arrhenius rate for the reaction $N(3) + e \rightarrow N(5) + e$	$4.9 \cdot 10^{-9} cm^3/s/part.$ +/- 1000%
N2 Quenching Prefactor~3-1-N	The prefactor of the Arrhenius rate for the reaction $N_2(B) + N \rightarrow N_2(X) + N$	$1 \cdot 10^{-10}\ cm^3/s/part.$ +/- 100%
N2 Quenching Exponent~3-1-N	The exponent of the Arrhenius rate for the reaction $N_2(B) + N \rightarrow N_2(X) + N$	0.5 +/- 0.5
N2 Quenching Exponent~3-1-N_2	The exponent of the Arrhenius rate for the reaction $N_2(B) + N_2 \rightarrow N_2(X) + N_2$	0.5 +/- 0.5

V. Conclusion

The objective of this work was to perform a series of spectral resolved sensitivity analyses of the DPLR-NEQAIR chemistry database across a variety of shock conditions in the EAST facility and perform a cursory comparison with experiments. DPLR in space marching mode and NEQAIR in shock tube mode were used to generate single realizations of the spectrum from a given chemical parameter sample. The chemical database was sampled and compiled by a new framework for storing generalized chemical data. The Sobol indices were calculated using an adaptive Monte Carlo strategy which used statistical bootstrapping to determine the most meaningful parameters to sample.

The Sobol indicies for a single shot across all spectral regions were presented. The most important parameters spanned both the DPLR database and the NEQAIR database. Although the DPLR rates were dominant across all regions, the relative order of the DPLR parameters differed region by region; furthermore, the NEQAIR parameters of importance changed completely across different spectral regions. This suggests that a spectrally resolved calibration based on these regions can more accurately tune individual state specific features. It was also noted that the electron impact ionization reaction was dominant, but continues to be inconsistently treated between DPLR and NEQAIR.

A comparison was then presented comparing the Sobol indices for the same shot and spectral region, but using an integrated radiance as the output vs a log-likelihood as an output. It was observed that the Sobol indices between the two were similar at all but the lowest presented indices. This indicates that the uncertainties in the DPLR chemical rates are acting in a global sense across the region as opposed to locally affecting spectral features such as line widths and band profiles. This effect was further confirmed by observing the spread in the integrated radiance over several regions. It was observed that in some regions and shots, the experimental data was outside the range of any of the chemical parameters. If the spectra is not close to the experimental data, the log-likelihood metric will not be substantially different from the difference in the integrated values.

The discrepancy itself represents critical information for the continuing effort to calibrate these chemical parameters. If no point in the sampling space matches EAST data, then certainly no physically meaningful calibration over that space is possible. This can be addressed by either widening the parameter uncertainties or by changing the underlying numerical model. Without further information it is not possible to determine which of those two options more physically consistent. Concurrent investigation into both possibilities is warranted for the future.

Acknowledgments

The authors would like to thank the NASA Entry Systems Modeling Project for the support of this work.

References

[1] Holloway, M. E., and Boyd, I. D., "Sensitivity Analysis of Thermochemical Kinetics Modeling for Hypersonic Air Flows," *Journal of Thermophysics and Heat Transfer*, Vol. 36, No. 3, 2022, pp. 584–593. https://doi.org/10.2514/1.T6427.

[2] Jo, S. M., Rostkowski, P., Doostan, A., Kim, J. G., and Panesi, M., "Influence of Non-Boltzmann Radiation around Titan Atmospheric Entry Vehicles," *AIAA AVIATION 2022 Forum*, American Institute of Aeronautics and Astronautics, 2022. https://doi.org/10.2514/6.2022-3576.

[3] Brandis, A., "Overview of Recent EAST Testing, Modeling & Analysis," , Apr. 2018.

[4] Brandis, A., Johnston, C., Cruden, B., Prabhu, D., and Bose, D., "Validation of High Speed Earth Atmospheric Entry Radiative Heating from 9.5 to 15.5 Km/s," *43rd AIAA Thermophysics Conference*, Fluid Dynamics and Co-located Conferences, American Institute of Aeronautics and Astronautics, 2012. https://doi.org/10.2514/6.2012-2865.

[5] Wright, M. J., White, T., and Mangini, N., *Data Parallel Line Relaxation (DPLR) Code User Manual: Acadia Version 4.01.1*, version 4.01.1 ed., No. 2009-215388 in NASA/TM, National Aeronautics and Space Administration, Ames Research Center, Moffett Field, Calif, 2009.

[6] Park, C., "Nonequilibrium Air Radiation (NEQAIR) Program : User's Manual," https://www.worldcat.org/title/nonequilibrium-air-radiation-neqair-program-users-manual/oclc/223882179?referer=di&ht=edition, ????

[7] Alkandry, H., Boyd, I. D., and Martin, A., "Comparison of Transport Properties Models for Flowfield Simulations of Ablative Heat Shields," *Journal of Thermophysics and Heat Transfer*, Vol. 28, No. 4, 2014, pp. 569–582. https://doi.org/10.2514/1.T4233.

[8] Gnoffo, P. A., Gupta, R. N., and Shinn, J. L., "Conservation Equations and Physical Models for Hypersonic Air Flows in Thermal and Chemical Nonequilibrium," 1989.

[9] Millikan, R. C., and White, D. R., "Systematics of Vibrational Relaxation," *The Journal of Chemical Physics*, Vol. 39, No. 12, 1963, pp. 3209–3213. https://doi.org/10.1063/1.1734182.

[10] Park, C., "Review of Chemical-Kinetic Problems of Future NASA Missions. I - Earth Entries," *Journal of Thermophysics and Heat Transfer*, Vol. 7, No. 3, 1993, pp. 385–398. https://doi.org/10.2514/3.431.

[11] Sobol', I. M., "Global Sensitivity Indices for Nonlinear Mathematical Models and Their Monte Carlo Estimates," *Mathematics and Computers in Simulation*, Vol. 55, No. 1, 2001, pp. 271–280. https://doi.org/10.1016/S0378-4754(00)00270-6.

[12] Saltelli, A., "Making Best Use of Model Evaluations to Compute Sensitivity Indices," *Computer Physics Communications*, Vol. 145, No. 2, 2002, pp. 280–297. https://doi.org/10.1016/S0010-4655(02)00280-1.

[13] Collen, P. L., Satchell, M., di Mare, L., and McGilvray, M., "Analysis of shock deceleration effects on radiation experiments in the NASA electric arc shock tube," *AIAA SciTech 2022 Forum*, 2022, p. 0267.